CHEMISTRY OF MATERIALS

pubs.acs.org/cm

Article

Ultrahigh Quantum Efficiency Near-Infrared-II Emission Achieved by Cr^{3+} Clusters to Ni^{2+} Energy Transfer

Chih-Yu Chang, Ming-Hsuan Huang, Kuan-Chun Chen, Wen-Tse Huang, Mikołaj Kamiński, Natalia Majewska, Tomasz Klimczuk, Jia-Hao Chen, Ding-Hua Cherng, Kuang-Mao Lu, Wei Kong Pang, Vanessa K. Peterson, Sebastian Mahlik,* Grzegorz Leniec,* and Ru-Shi Liu*

Cite This: *Chem. Mater.* 2024, 36, 3941−3948

Read Online

ACCESS | Metrics & More | Article Recommendations | Supporting Information

ABSTRACT: Increasing demand for near-infrared-II (NIR-II) light sources requires improved NIR-II phosphors. We present a series of phosphors codoped with Cr^{3+} and Ni^{2+} that possess NIR-II emission with an unprecedented internal quantum efficiency (IQE) of 97.4%. Our study reveals an energy transfer mechanism involving clusters of Cr^{3+} where luminescent centers are closely matched in energy and where the Ni^{2+} emission intensity can be tuned through sintering temperature. The profound electron paramagnetic resonance (EPR) studies disclose the interaction between Cr^{3+} clusters and Cr^{3+}−Ni^{2+} pairs, further proving the cause of such a high IQE and the significance of Cr^{3+} clusters. This work provides promising pathways for the development of NIR-II light-emitting diodes with outstanding efficiency by suggesting a new energy transfer source of Cr^{3+}.

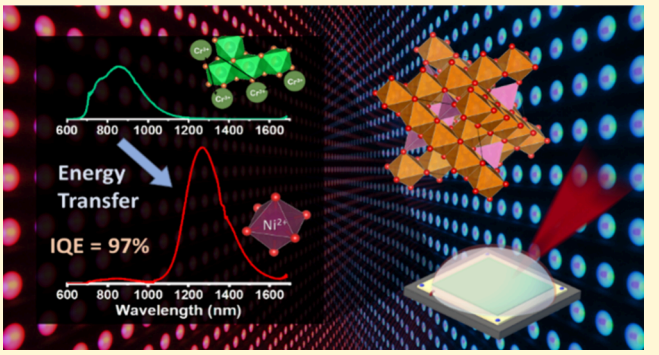

INTRODUCTION

The near-infrared-II (NIR-II) emission region, lying between 1000 and 1700 nm,[1] is favored for sensing applications due to low scattering, deep penetration, and high signal-to-background ratio, enabling sensitive chemical bond detection. The NIR-II emission region has, therefore, been widely exploited for bioimaging, biodetection, noninvasive biotreatments, and nondestructive food analysis,[2−5] leading to increasing demand for phosphor-converted light-emitting diodes (pc-LEDs) with NIR-II emission.[6]

Transition metal and lanthanoid elements, such as Cr^{3+}, Cr^{4+}, Mn^{4+}, Ni^{2+}, Eu^{2+}, Er^{3+}, and Yb^{3+}, are commonly used activators for NIR emission.[7−12] Among these, Ni^{2+} exhibits broadband emission in the NIR-II region, with the emission range tunable through the crystal field.[13] However, the typical Ni^{2+} excitation sources such as 808/980 nm lasers and ultraviolet (UV)/near UV chips are energy-inefficient, suffering from low quantum efficiency.[14,15] Wang et al.[16] reported a series of Cr^{3+}/Ni^{2+} codoped NIR phosphors $Zn_{1+y}Sn_yGa_{2-2y}O_4$ with a Ni^{2+} emission intensity that can be enhanced by 450 nm blue light excitation, achieved through Cr^{3+}−Ni^{2+} electric dipole−dipole interactions, opening a new approach for NIR-II phosphor design. Single Cr^{3+} to Ni^{2+} energy transfer has been reported widely, with an internal quantum efficiency (IQE) of approximately 50%,[5,17−19] with a higher IQE of approximately 70% reported through energy transfer from Cr^{3+}−Cr^{3+} ion pairs to Ni^{2+}.[20] Notably, the most efficient Cr^{3+}−Ni^{2+} energy transfer in the $Zn_{1+y}Sn_yGa_{2-2y}O_4$ phosphor series codoped with Cr^{3+}/Ni^{2+} was found for compositions with an intermediate spinel-type structure, found between normal and inverse spinel-type structures.[16] Miao et al.[21] reported the intermediate spinel-type structured phosphor $MgGa_2O_4$:Cr^{3+},Ni^{2+} with an ultrahigh IQE of 96.5%; however, the structural properties and luminescent mechanism were not investigated. Focusing on the $MgGa_2O_4$ system, Yao et al.[22] reported the likely existence of Cr^{3+}−Cr^{3+} ion pairs in the $MgGa_2O_4$ intermediate spinel-type structure, and Rajendran et al.[23] reported the presence of Cr^{3+} clusters in an intermediate spinel-type structured material. Therefore, our work leverages insights into the high-efficiency energy transfer from Cr^{3+} clusters to Ni^{2+} in the intermediate spinel $MgGa_2O_4$ structure to achieve ultrahigh IQE in the NIR-II region.

The present work investigates the energy transfer from single Cr^{3+} ions ($x = 0.02$) and Cr^{3+} clusters ($x = 0.06$) to Ni^{2+} in the $Mg_{1-y}Ga_{2-x}O_4$:xCr^{3+},yNi^{2+} series with an intermediate spinel-type structure. We report detailed crystal structural analysis and luminescence properties, as well as energy transfer

Received: February 21, 2024
Revised: April 2, 2024
Accepted: April 2, 2024
Published: April 12, 2024

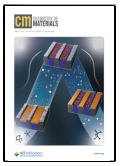

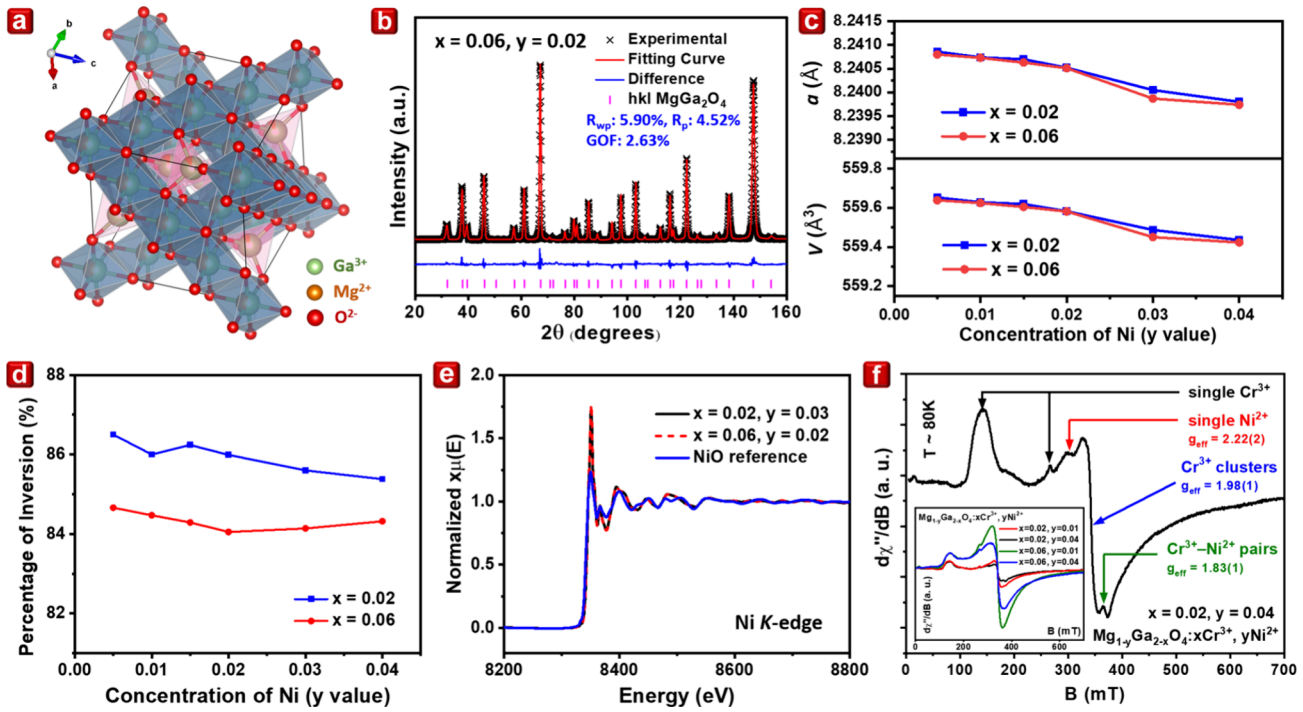

Figure 1. Structural characterization of $Mg_{1-y}Ga_{2-x}O_4$:xCr^{3+},yNi^{2+}. (a) Crystal structure of $MgGa_2O_4$ (ICDD #1252694) with space group symmetry of $Fd\bar{3}m$. Octahedrons are colored in blue, and tetrahedrons are colored in pink; green atoms are the percentages occupied by Ga^{3+}, orange atoms are the percentages occupied by Mg^{2+}, and red atoms are those occupied by O^{2-}. (b) Rietveld refinement profile using neutron powder diffraction data (jointly refined against synchrotron X-ray powder diffraction shown in Figure S3) of $Mg_{1-y}Ga_{2-x}O_4$:xCr^{3+},yNi^{2+} at $x = 0.06$ and $y = 0.02$. The figures of merit are the profile R-factor R_p, the weighted profile R-factor R_{wp}, and the goodness of fit (GOF). (c) Lattice parameter and volume and (d) calculated percentage of inversion of the $Mg_{1-y}Ga_{2-x}O_4$:xCr^{3+},yNi^{2+} series. Lines through points guide the eye, and errors are smaller than the points. (e) Ni K-edge XANES data of $Mg_{1-y}Ga_{2-x}O_4$:xCr^{3+},yNi^{2+} for $x = 0.02$, $y = 0.03$ and $x = 0.06$, $y = 0.02$ samples, along with the NiO reference. (f) EPR data for $Mg_{1-y}Ga_{2-x}O_4$:xCr^{3+},yNi^{2+} at 80 K, where g_{eff} is the effective value of the spectroscopic splitting ratio.

mechanisms, unveiling the importance of Cr^{3+} clusters in achieving high-efficiency NIR-II emission.

RESULTS AND DISCUSSION

Structural Analysis. $MgGa_2O_4$ has an intermediate spinel-type crystal structure with an $Fd\bar{3}m$ space group comprising six coordinate octahedra (M1) and four coordinate tetrahedra (M2) in the ratio 2 to 1, shown in blue and pink, respectively, in Figure 1a. This structure has M1 and M2 occupied by both Mg^{2+} and Ga^{3+} and can therefore host codoped Cr^{3+} (substituting Ga^{3+}) and Ni^{2+} (substituting Mg^{2+}, yielding luminescence[24,25]) to form $Mg_{1-y}Ga_{2-x}O_4$:xCr^{3+},yNi^{2+}.

$Mg_{1-y}Ga_{2-x}O_4$:xCr^{3+},yNi^{2+} with $x = 0.02$, $y = 0.005-0.04$ and $x = 0.06$, $y = 0.005-0.04$ were characterized using laboratory powder X-ray diffraction (XRD) shown in Figure S1. The samples show high crystallinity, and all peaks could be indexed to the $MgGa_2O_4$ structure (ICDD #1252694), indicating phase purity. Rietveld refinement of this structure using synchrotron XRD (S-XRD) (and jointly against neutron powder diffraction (NPD) data for the $x = 0.06$, $y = 0.02$ composition) is shown in Figure 1b, Figures S2 and S3, and Tables S1−S4, where the figures of merit the profile R-factor (R_p), the weighted profile R-factor (R_{wp}), and the goodness of fit (GOF) indicate reliable results.[26] The refined unit cell parameter a and the unit cell volume V decrease with increasing Ni^{2+} concentration in samples with $x = 0.02$ and 0.06, as shown in Figure 1c. The decrease in a with increased Ni^{2+} is expected as a result of the smaller Ni^{2+} relative to Mg^{2+}, where Mg^{2+}(VI) has an ionic radius of 0.72 Å and Ni^{2+}(VI) of 0.69 Å, compared with Ga^{3+}(VI) of 0.62 Å.[27] Notably, if Ni^{2+} ions were to substitute Ga^{3+}, an increase in a is expected. The difference in a for samples with the same concentrations of Ni^{2+} but different Cr^{3+} originates from the substitution of Ga^{3+} by slightly smaller Cr^{3+}(VI) with a radius of 0.615 Å.[27]

Different occupancies of M1 and M2 by different cations are found, and the degree of inversion is calculated in Figure 1d, specifically determining the percentage of trivalent cations in the M2 tetrahedral site.[28] Both series maintained a high degree of inversion for the system of around 86 and 84% for low and high Cr^{3+} concentration samples, respectively. This reveals that the octahedral M1 site consists of around 43% of the divalent environment, where Ni^{2+} is substituted in the octahedral site, which leads to a likelihood of fewer defects.

Cr and Ga are hard to distinguish using X-ray diffraction, especially given the small Cr concentration. For this reason, we used the NPD data of the $x = 0.06$, $y = 0.02$ composition sample to determine that Cr^{3+} occupies predominantly the octahedral M1 site substituting Ga^{3+}. X-ray absorption near-edge structure (XANES) measurements at the Ni K-edge for the $x = 0.02$, $y = 0.03$ and $x = 0.06$, $y = 0.02$ samples are shown in Figure 1e,[29] along with the NiO standard, revealing similar valencies of Ni^{2+}. No pre-edge is found for either sample, indicating a more symmetric, octahedral environment.[30] In all, we conclude that the system contains predominantly Ni^{2+} in the octahedral M1 site. The Cr XANES analysis is presented in the Supporting Information.

Electron paramagnetic resonance (EPR) studies were conducted to investigate the environment and interactions of

https://doi.org/10.1021/acs.chemmater.4c00438
Chem. Mater. 2024, 36, 3941−3948

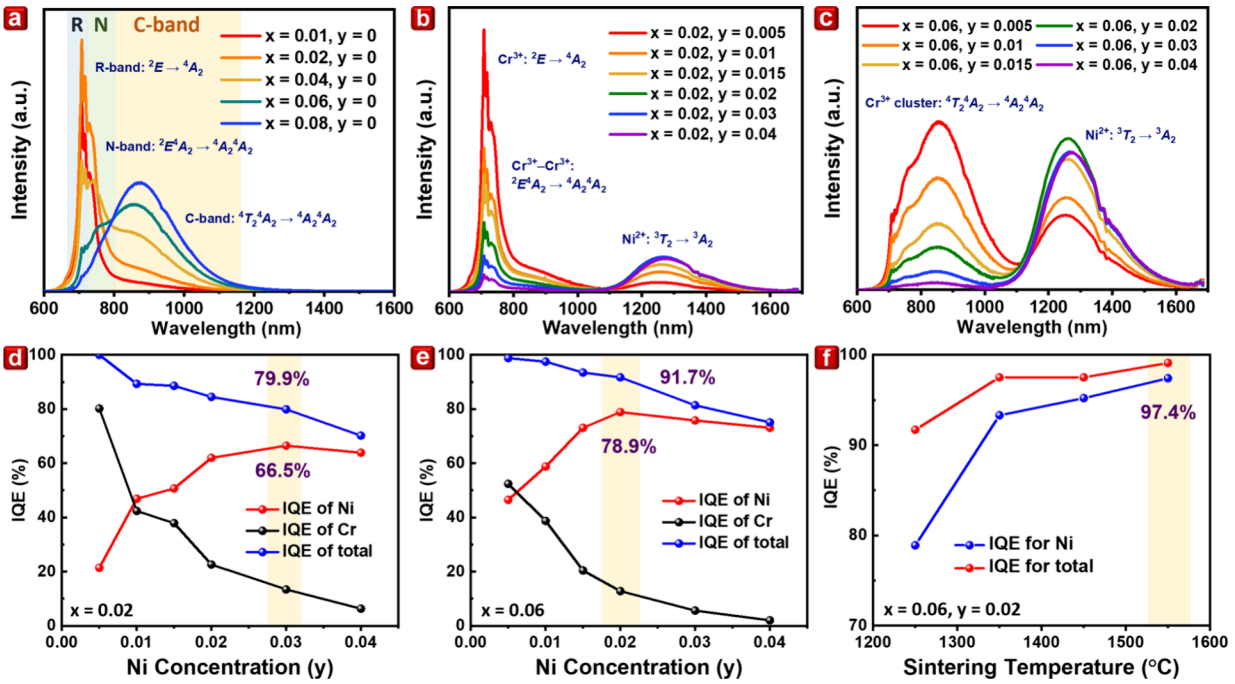

Figure 2. Photoluminescence properties of $Mg_{1-y}Ga_{2-x}O_4$:xCr^{3+},yNi^{2+} at room temperature. PL spectra upon excitation at 460 nm of (a) $x = 0.01-0.08$, $y = 0$, (b) $x = 0.02$, $y = 0.005-0.04$, and (c) $x = 0.06$, $y = 0.005-0.04$ with marked energy level transitions. Internal quantum efficiency (IQE) of (d) $x = 0.02$, $y = 0.005-0.04$, (e) $x = 0.06$, $y = 0.005-0.04$, and (f) $x = 0.06$, $y = 0.02$ at different sintering temperatures. Lines through the points are guides to the eye. R, N, and C band emissions are shaded in blue, green, and orange, respectively.

the paramagnetic luminescent centers.[31,32] Cr^{3+} ions have spin $S = 3/2$, and EPR spectra are recorded over the full temperature range, while Ni^{2+} ions have integer spin $S = 1$. Thus, the EPR signal from Ni^{2+} can be observed only at low temperatures. Figure 1f shows the EPR spectrum for a selected $Mg_{1-y}Ga_{2-x}O_4$:xCr^{3+},yNi^{2+} compound at $T \approx 80$ K in the range of up to 700 mT. In the EPR signal, it is possible to distinguish EPR lines originating from single Cr^{3+}, single Ni^{2+}, Cr^{3+} clusters, and Cr^{3+}–Ni^{2+} ion pairs, with the effective spectroscopic splitting ratio $g_{eff} = 4.74/2.54$, 2.22, 1.98, and 1.83, respectively.[33−35] The presence of Cr^{3+} clusters has been found and investigated by Rajendran et al.[23] The samples are reproduced and measured in Figure S5a and fitted using the Curie–Weiss model for single Cr^{3+} and the Bleaney–Bowers (BB) model for Cr^{3+} clusters.[36,37] The Ni^{2+}-doped-only samples are also synthesized and measured at 80 K in Figure S5b. The results indicate that the signal originates from a single Ni^{2+} in the octahedral site rather than NiO, where Ni^{2+} ions strongly interact with each other and where the intensity of the signal increases with increased Ni^{2+} concentration.[38] A decrease in the Cr^{3+} cluster signal is observed on the increasing concentration of Ni^{2+}, shown in the inset in Figure 1f and Figure S6a,b. However, this intensity decrease was not accompanied by the broadening of the signal, as shown in Figure S5a, with a change in only the concentration of Cr^{3+}. Therefore, all spin Hamiltonian (SH) parameter fittings were conducted for experimental data as shown in Figures S5c,d and S6c,d. It should be noted that the signals from single Ni^{2+} ions are in superposition with the signals from Cr^{3+} clusters. At the same time, the signal from single Ni^{2+} ions is left of the signal from Cr^{3+} clusters, and the signal from Cr^{3+}–Ni^{2+} ion pairs is right of the signal from Cr^{3+} clusters. The negative part of the signal from single Ni^{2+} ions aligns with the maximum of the positive part of the Cr^{3+} clusters, while the positive part of the Cr^{3+}–Ni^{2+} signal aligns with the maximum of the negative part of the signal from Cr^{3+} clusters. Hence, the decrease in the Cr^{3+} cluster signal does not originate from a decrease in Cr^{3+} cluster formation but from the superposition of multiple signals. This also indicates that Ni^{2+} substitutes in an environment that is different from that of Cr^{3+}. No evidence of crystal lattice defects was observed in either EPR signal ($g_{eff} \approx 2$) or SH fitting parameters,[39] suggesting that Ni^{2+} substitutes at the octahedral Mg^{2+} site with the same ionic valency, similar ionic radii, and suitable symmetric environment, reinforcing the nominal chemical formula. Temperature-dependent magnetic susceptibility (MS) is shown in Figure S7 and confirms the EPR results.

Photoluminescence (PL). Basic luminescence properties of single-doped Cr^{3+} and Ni^{2+} in the $MgGa_2O_4$ structure were reported previously by Rajendran et al.[23] and Suzuki et al.,[40] and therefore, we focus on the codoped system. The photoluminescence (PL) spectrum of single-doped Cr^{3+} samples is shown in Figure 2a as a function of the Cr^{3+} doping. The emission spectrum consists of three bands, the R-band (708 nm), the N-band (750 nm), and the C-band (850 nm), arising from the emission of single Cr^{3+}, Cr^{3+}–Cr^{3+} pairs, and Cr^{3+} clusters, respectively.[23] The IQE of the samples is listed in Table S5, where an IQE > 97% up to $x = 0.06$ is found. Based on this result, the $x = 0.02$ and $x = 0.06$ compositions are identified as low and high Cr^{3+} concentration groups for our Cr^{3+} to Ni^{2+} energy transfer research targeting the energy transfer mechanism from single Cr^{3+} and Cr^{3+} clusters.

The photoluminescence excitation (PLE) spectra of both series $Mg_{1-y}Ga_{2-x}O_4$:xCr^{3+},yNi^{2+}, $x = 0.02$, $y = 0.005-0.04$ and $x = 0.06$, $y = 0.005-0.04$ are shown in Figure S8. For samples with $x = 0.02$, upon 708 nm observation (corresponding to the $^2E \rightarrow {}^4A_2$ transition of Cr^{3+}), the PLE

https://doi.org/10.1021/acs.chemmater.4c00438
Chem. Mater. 2024, 36, 3941−3948

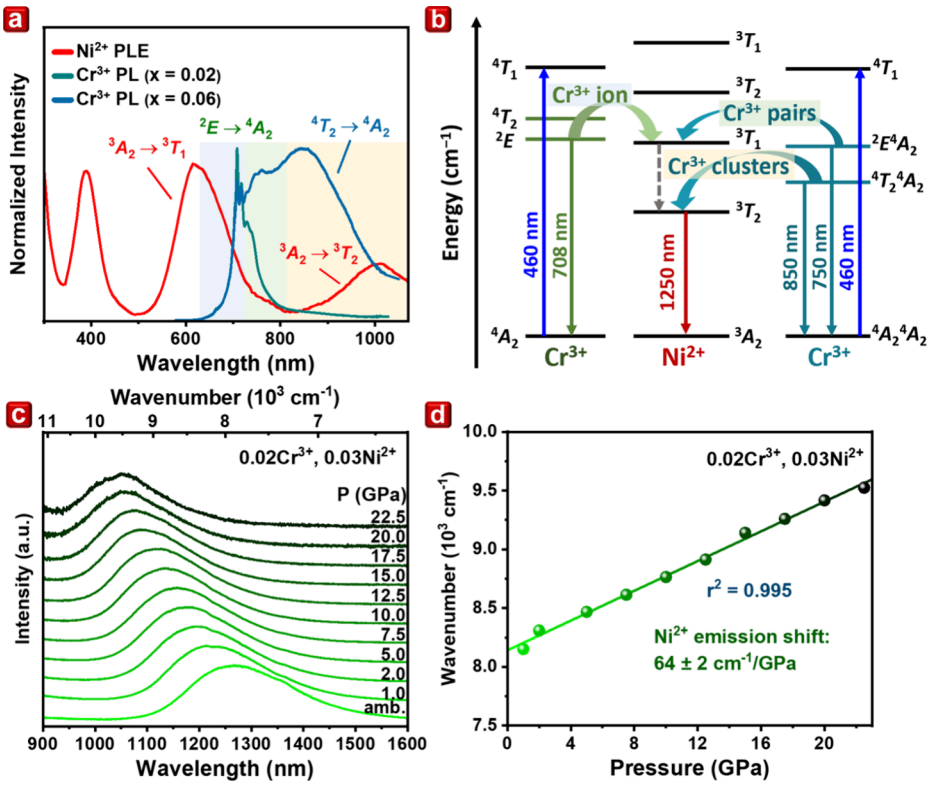

Figure 3. Energy transfer mechanism. (a) PL spectrum of $Mg_{1-y}Ga_{2-x}O_4{:}xCr^{3+},yNi^{2+}$, $x = 0.02$, $y = 0$ and $x = 0.06$, $y = 0$ upon excitation at 420 nm, and the PLE spectrum of $x = 0$, $y = 0.005$ monitored at 1250 nm. The intensities are normalized with transitions identified. (b) Schematic of energy levels and the energy transfer mechanism for isolated Cr^{3+} and Cr^{3+} pairs and clusters. Pressure studies were performed for $Mg_{1-y}Ga_{2-x}O_4{:}xCr^{3+},yNi^{2+}$. (c) Pressure-dependent PL spectra for $Mg_{1-y}Ga_{2-x}O_4{:}xCr^{3+},yNi^{2+}$, $x = 0.02$, $y = 0.03$ excited at 442 nm from ambient pressure to 22.5 GPa, and (d) peak energy of emission with pressure.

spectra consist of two excitation bands typical for Cr^{3+} in 6-fold octahedral coordination. The high energy band at 420 nm corresponds to the $^4A_2 \rightarrow {}^4T_1$ transition. In contrast, the lower energy band at 580 nm is related to the $^4A_2 \rightarrow {}^4T_2$ transition of Cr^{3+}. Upon excitation of 460 nm, the PL spectrum can be divided into two regions, short wavelength and long wavelength, arising from Cr^{3+} and Ni^{2+}, respectively, as shown in Figure 2b. The emission from Cr^{3+} consists of the R-band, corresponding to the $^2E \rightarrow {}^4A_2$ transition, and the N-band, from Cr^{3+}–Cr^{3+} pairs luminescence. The emission from Ni^{2+} (1100–1600 nm) corresponds to the $^3T_2 \rightarrow {}^3A_2$ transition with a maximum at 1260 nm and full-width at half-maximum (fwhm) of ≈210 nm, consistent with the results of Miao et al.[21] The concentration of Ni^{2+} does not affect the shape of Cr^{3+} and Ni^{2+} excitation and emission spectra, but enhances the intensity of Ni^{2+} while lowering the emission of Cr^{3+} significantly. The IQE is given in Table S6 and Figure 2d. The IQE of Cr^{3+} decreased and of Ni^{2+} increased until $y = 0.03$, with the highest IQE = 66.5% for the low Cr^{3+} concentration series ($x = 0.02$).

For the high Cr^{3+} concentration samples ($x = 0.06$), the PLE is shown in Figure S8b is the same as the low Cr^{3+} concentration series, while the PL is remarkably different, as shown in Figure 2c. Though the PL spectrum is also divided into two regions, the emission from Cr^{3+} is dominated by the N-band and C-band, arising from the emission of the induced Cr^{3+}–Cr^{3+} pair and Cr^{3+} clusters at high Cr^{3+} concentration, while the R-band of Cr^{3+} is still observed but much less intense by comparison. The concentration of Ni^{2+} does not change the shape of the Cr^{3+} and Ni^{2+} excitation and emission spectra. As the concentration of Ni^{2+} increases, the emission intensity of Ni^{2+} is enhanced, whereas the emission intensity of Cr^{3+} declines, which may indicate more efficient energy transfer through Cr^{3+} clusters. The IQE values are listed in Table S7 and plotted in Figure 2e, with the IQE of Cr^{3+} decreasing and of Ni^{2+} increasing until $y = 0.02$, yielding a maximum IQE = 78.9% for the highest Cr^{3+} concentration ($x = 0.06$), with the intensity drop for Ni^{2+} at $y > 0.02$ suggesting concentration quenching.

The highest IQE arising from Ni^{2+} emission was obtained for $Mg_{1-y}Ga_{2-x}O_4{:}xCr^{3+},yNi^{2+}$, $x = 0.06$, $y = 0.02$, and we investigated the PL of this sample as a function of sintering temperature in the range 1250 to 1550 °C due to instrument constraints. The PL results show the emission intensity of Cr^{3+} drops, and the intensity of Ni^{2+} increases with increased sintering temperature, as shown in Figure S9, with IQE shown in Table S8 and Figure 2f resulting in an IQE from Ni^{2+} emission as high as 97.4% at the sintering temperature of 1550 °C. The cause of such phenomenon originates from the increased grain size observed in the SEM images and particle analysis, as shown in Figure S10 and Table S9, while larger grain size suppresses the formation and possibility of defects due to smaller surface area. This obtained IQE is higher than that of any reported phosphor emission in the NIR-II region to date.

Energy Transfer Mechanism. To understand the energy transfer mechanism in the system that gives out such high IQEs, the PLE and PL spectra of single-doped Ni^{2+} samples ($Mg_{1-y}Ga_{2-x}O_4{:}xCr^{3+},yNi^{2+}$, $x = 0$, $y = 0.005$–0.04) are shown in Figure S11. Upon observation at 1250 nm, PLE spectra

https://doi.org/10.1021/acs.chemmater.4c00438
Chem. Mater. 2024, 36, 3941–3948

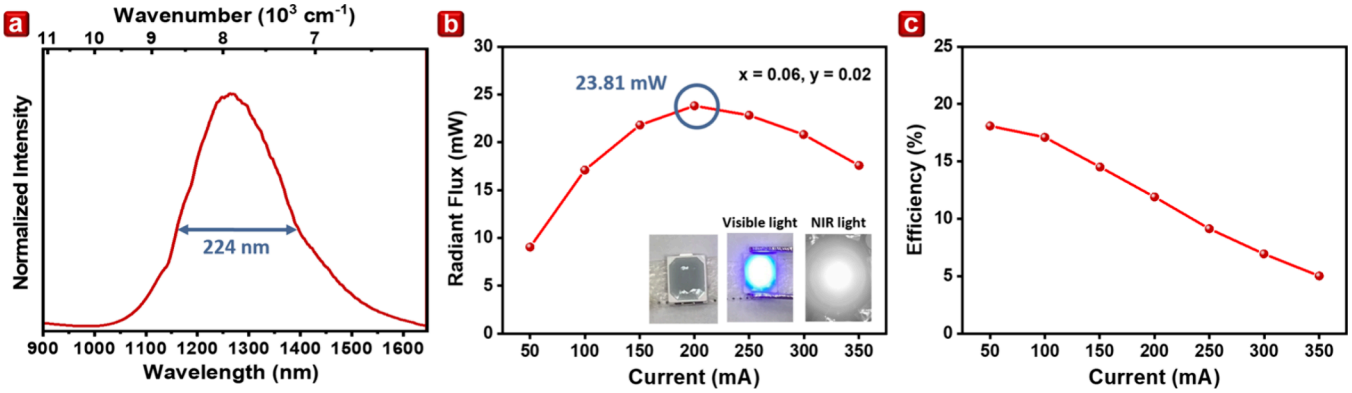

Figure 4. LED performance test results. (a) Emission spectrum (fwhm = full width at half-maximum = 224 nm), (b) radiant flux, and (c) efficiency of NIR pc-LEDs containing $Mg_{1-y}Ga_{2-x}O_4$:xCr^{3+},yNi^{2+}, $x = 0.06$, $y = 0.02$. A photo of the LED device is shown in the inset, with the appearance of the working LED device under visible and NIR light.

consist of three excitation bands at 390, 630, and 1000 nm, corresponding to the transitions $^3A_2 \rightarrow {}^3T_1$ (^3P), $^3A_2 \rightarrow {}^3T_1$ (^3F), and $^3A_2 \rightarrow {}^3T_2$ (^3F), respectively, for octahedrally coordinated Ni^{2+} ions,[41,42] where no excitation peaks match the energy of our excitation at 460 nm in the PLE spectrum of Ni^{2+}. Figure 3a shows the PLE of Ni^{2+} along with the PL of low and high Cr^{3+} concentration samples, where blue shading indicates the R-band, green shading the N-band, and orange shading the C-band. The R- and N-bands correspond to the $^3A_2 \rightarrow {}^3T_1$ (^3F) transition of Ni^{2+}, while the C-band corresponds to the $^3A_2 \rightarrow {}^3T_2$ (^3F) transition of Ni^{2+}, indicating possible energy transfer between the activators.

The proposed energy transfer mechanism is shown in Figure 3b. The energy levels of Ni^{2+} in an octahedral environment are fixed centrally, with those of single Cr^{3+} on the left and pair/cluster Cr^{3+} on the right. Upon 460 nm blue light excitation, single Cr^{3+} can be excited to the $^4T_1$ state, where electrons nonradiatively relax to the lowest excited state ^2E before emitting 708 nm light (R-band). Simultaneously, energy is transferred to Ni^{2+} at the $^3T_1$ energy level, also followed by a nonradiative transition to the lowest excited state, $^3T_2$, before producing 1250 nm NIR-II light. Cr^{3+}−Cr^{3+} pairs and Cr^{3+} clusters can also be excited by 460 nm blue light, resulting in 750 nm (N-band) and 850 nm (C-band) emission, distributing to $Ni^{2+3}T_1$ and $^3T_2$ energy levels, respectively. Since energy transfer from Cr^{3+} clusters to the $^3T_2$ energy level of Ni^{2+} occurs directly and does not require nonradiative transition before emitting NIR-II light, it is reasonable that such a transfer process would be highly efficient.

The efficiencies are calculated for the series through the eq 1 below:

$$\eta_T = 1 - \frac{I_S}{I_0} \quad (1)$$

where I_0 and I_S are the Cr^{3+} emission intensities in the absence and presence of Ni^{2+}, respectively,[16] obtained from Tables S5−S8. Since several luminescent centers participated in the energy transfer process (Cr^{3+} ions, Cr^{3+}−Cr^{3+} pairs, and Cr^{3+} clusters), multiple decay pathways were present. Therefore, it is unreliable to calculate the energy efficiency solely by the decay curve since decay times are observed as average decay times and do not represent any individual luminescent centers. The energy transfer efficiency is found to increase with the concentration of Ni^{2+} for both series, with the values of $x = 0.06$ being higher throughout, reaching a maximum of 93.6 and 98.0% for samples $x = 0.02$, $y = 0.04$, and $x = 0.06$, $y = 0.04$, respectively, as shown in Figure S12a. Such high energy transfer efficiency can be attributed to the interactions of Cr^{3+}−Ni^{2+} pairs detected through EPR. Therefore, along with the IQE findings, we suggest that it is more effective for Cr^{3+} clusters to transfer their energy to the Ni^{2+} luminescent center than single Cr^{3+} ions. As expected, the energy transfer efficiency increases with sintering temperature due to the higher IQE, shown in Figure S12b, resulting in a maximum of 98.3% at 1550 °C. However, the trend of IQE does not match that of the energy transfer efficiency for the $x = 0.02$, $y = 0.005$−0.04 and $x = 0.06$, $y = 0.005$−0.04 series at a sintering temperature of 1250 °C, possibly attributable to concentration quenching and energy loss in the nonradiative relaxation process in the Ni^{2+} system.

Energy transfer and concentration quenching are also supported by the decay profiles shown in Figures S13 and S14. The detailed calculation of the decay profiles is elaborated in the Supporting Information. The calculated decay time for Cr^{3+} is much shorter for samples with $x = 0.06$ (0.5 ms for $y = 0$) compared to samples with $x = 0.02$ (4.3 ms for $y = 0$). The decay time also decreases with increasing the y for both series, from 4.3 to 2.8 ms for samples with $x = 0.02$ and from 0.5 to 0.29 ms for samples with $x = 0.06$. With the decay profiles of Cr^{3+} emission being multiexponential for all samples and shortening with increasing y, this supports the above-mentioned energy transfer mechanism. It is shown that the line and broadband emissions arise from the two different luminescence sites, from single Cr^{3+} and from interacting Cr^{3+}, and shortening of the decay time may arise from energy transfer between the two luminescence sites. Alternatively, concentration quenching may also contribute to the reduced decay time.

Thermal and Pressure Studies. The temperature-dependent studies are elaborated in the Supporting Information. Both samples show stable emission intensity up to 250 K followed by an obvious decrease, with 47.5% and 44.5% remaining intensity at the 423 K LED device working temperature for $x = 0.02$, $y = 0.03$, and $x = 0.06$, $y = 0.02$, respectively, indicating slightly better thermal stability for the $x = 0.02$, $y = 0.03$ sample. The reason for this is that Cr^{3+} clusters encompass poorer thermal stability; therefore, the intensity drops slightly more significantly for Cr^{3+} cluster-induced NIR-II phosphors at rising temperatures.

https://doi.org/10.1021/acs.chemmater.4c00438
Chem. Mater. 2024, 36, 3941−3948

The pressure-dependent PL spectra of Ni^{2+} emission up to 22.5 GPa for sample $x = 0.02$, $y = 0.03$ are shown in Figure 3c. The reason for demonstrating the $x = 0.02$, $y = 0.03$ sample rather than the $x = 0.06$, $y = 0.02$ sample is because the emission spectrum of Cr^{3+} clusters overlaps the monitored Ni^{2+} emission spectrum. Henceforth, sample $x = 0.02$, and $y = 0.03$ would be a better candidate for investigating the emission performance to pressure. The shape of the spectrum in Figure 3c remains unchanged as the applied pressure increases, but there is a noticeable shift in position toward higher energies. By applying pressure to the samples, the strength of the crystal field increases, resulting in a shift of the $^3T_2$ level toward higher energy. A pressure-induced shift of 1268 cm^{-1} is found from ambient pressure to 22.5 GPa, with the peak position changing from 1272 to 1050 nm. The band position is plotted with applied pressure in Figure 3d, where the shift is linearly correlated with the pressure at 64 ± 2 cm^{-1}/GPa. Though the significance of pressure change in LED performance is relatively low, such linearity is helpful in future NIR pressure sensing applications.

LED Performance. Sample of $Mg_{1-y}Ga_{2-x}O_4{:}xCr^{3+},yNi^{2+}$, $x = 0.06$, $y = 0.02$ was used to fabricate a 2835 NIR phosphor-converted (pc) light emitting diode (LED) by coating the phosphors onto a blue LED chip with an emission wavelength of 452 nm as a light source. The emission spectrum, radiant flux, and blue light conversion efficiency are listed in Figure 4. The resulting emission from Ni^{2+} powered by the blue LED chip ranges over 1000−1600 nm in the NIR-II region, peaking at 1265 nm, with a maximum radiant flux of 23.81 mW at 200 mA driving current. The blue light conversion efficiency decreased over a higher current, leaving 11.9% at a 200 mA driving current. The device is shown in the inset of Figure 4b, and the outstanding luminescent performance results reveal this phosphor series possesses great potential for future applications.

CONCLUSIONS

In summary, our study on the energy transfer mechanism of the intermediate spinel $MgGa_2O_4$ crystal codoped with Cr^{3+} and Ni^{2+} has shed light on the potential for achieving near-unity quantum efficient NIR-II emission for pc-LEDs. Diffraction analyses confirm the crystal structures of the synthesized samples and the substitution of Cr^{3+} for Ga^{3+} at octahedral M1 sites. EPR studies reveal the presence of Cr^{3+} clusters, the successful substitution of Ni^{2+} for octahedral Mg^{2+}, and a strong Cr^{3+}−Ni^{2+} pair interaction. PL measurements demonstrate emission from both luminescent centers, and an energy transfer mechanism is proposed that involves energy transfer from Cr^{3+} and Cr^{3+} clusters to Ni^{2+}. Further, the sintering temperature can be used to tune and enhance the Ni^{2+} emission intensity, resulting in an unprecedented NIR-II emission IQE of 97.4%. The insights gained from this study contribute to a deeper understanding of energy transfer mechanisms involving Cr^{3+} clusters, opening new possibilities for developing highly efficient and high-performance LEDs operating in the NIR-II window.

EXPERIMENTAL SECTION

Reagents. Gallium oxide (Ga_2O_3, 99.9%) was purchased from Gredmann; magnesium oxide (MgO, 99.9%) and chromium oxide (Cr_2O_3, 99.9%) were purchased from Merck; nickel oxide (NiO, 97%) was purchased from Acros.

Synthesis of $Mg_{1-y}Ga_{2-x}O_4{:}xCr^{3+},yNi^{2+}$ ($x = 0.02/0.06$, $y = 0.005-0.04$). The material was synthesized by using a solid-state reaction method. The precursors were weighed according to stoichiometric ratios and ground in an agate mortar for 20 min. The mixed powders were transferred into an alumina crucible and sintered at 1250 to 1550 °C for 5 h in the air. Finally, the sintered powders were ground in an agate mortar and pestle again. Further characterization and experimental measurements are provided in the Supporting Information.

ASSOCIATED CONTENT

Supporting Information

The Supporting Information is available free of charge at https://pubs.acs.org/doi/10.1021/acs.chemmater.4c00438.

Details of characterization, Rietveld fit profiles along with refined structural parameters, electron paramagnetic resonance profiles, pressure-dependent decay profiles and calculated decay time, temperature-dependent emission spectra, and decay profiles (PDF)

AUTHOR INFORMATION

Corresponding Authors

Sebastian Mahlik − *Institute of Experimental Physics, Faculty of Mathematics, Physics, and Informatics, University of Gdansk, Gdańsk 80-308, Poland;* orcid.org/0000-0002-9514-049X; Email: sebastian.mahlik@ug.edu.pl

Grzegorz Leniec − *Department of Nanomaterials Physicochemistry, Faculty of Chemical Technology and Engineering, West Pomeranian University of Technology in Szczecin, Szczecin 70-311, Poland;* Email: Grzegorz.Leniec@zut.edu.pl

Ru-Shi Liu − *Department of Chemistry, National Taiwan University, Taipei 106, Taiwan;* orcid.org/0000-0002-1291-9052; Email: rsliu@ntu.edu.tw

Authors

Chih-Yu Chang − *Department of Chemistry, National Taiwan University, Taipei 106, Taiwan*

Ming-Hsuan Huang − *Department of Chemistry, National Taiwan University, Taipei 106, Taiwan*

Kuan-Chun Chen − *Department of Chemistry, National Taiwan University, Taipei 106, Taiwan*

Wen-Tse Huang − *Department of Chemistry, National Taiwan University, Taipei 106, Taiwan*

Mikołaj Kamiński − *Institute of Experimental Physics, Faculty of Mathematics, Physics, and Informatics, University of Gdansk, Gdańsk 80-308, Poland*

Natalia Majewska − *Institute of Experimental Physics, Faculty of Mathematics, Physics, and Informatics, University of Gdansk, Gdańsk 80-308, Poland;* orcid.org/0000-0002-1933-0355

Tomasz Klimczuk − *Faculty of Applied Physics and Mathematics and Advanced Materials Centre, Gdansk University of Technology, Gdańsk 80-233, Poland;* orcid.org/0000-0002-7089-4631

Jia-Hao Chen − *Everlight Electronics Co., Ltd., New Taipei City 238, Taiwan*

Ding-Hua Cherng − *Everlight Electronics Co., Ltd., New Taipei City 238, Taiwan*

Kuang-Mao Lu − *Everlight Electronics Co., Ltd., New Taipei City 238, Taiwan*

Wei Kong Pang − *Institute for Superconducting and Electronic Materials, University of Wollongong, North Wollongong, New*

South Wales 2500, Australia; orcid.org/0000-0002-5118-3885

Vanessa K. Peterson − *Institute for Superconducting and Electronic Materials, University of Wollongong, North Wollongong, New South Wales 2500, Australia; Australian Centre for Neutron Scattering, Australian Nuclear Science and Technology Organisation, Sydney, New South Wales 2232, Australia*

Complete contact information is available at: https://pubs.acs.org/10.1021/acs.chemmater.4c00438

Author Contributions

The manuscript was written with contributions from all authors. All authors have given approval to the final version of the manuscript.

Notes

The authors declare no competing financial interest.

■ ACKNOWLEDGMENTS

This work was financially supported by the Ministry of Science and Technology in Taiwan (contract nos. NSTC 112-2113-M-002-020 and NSTC 113-2923-M-002-006), the National Science Center Poland Grant Opus No. 2018/31/B/ST4/00924, and the National Centre for Research and Development Poland Grant No. PL-TW/VIII/1/2021. NPD data on Echidna were collected under proposal MI13201.

■ REFERENCES

(1) Antaris, A. L.; Chen, H.; Cheng, K.; Sun, Y.; Hong, G.; Qu, C.; Diao, S.; Deng, Z.; Hu, X.; Zhang, B.; Zhang, X.; Yaghi, O. K.; Alamparambil, Z. R.; Hong, X.; Cheng, Z.; Dai, H. A Small-Molecule Dye for NIR-II Imaging. *Nat. Mater.* **2016**, *15*, 235−242.

(2) Chen, Y.; Xue, L.; Zhu, Q.; Feng, Y.; Wu, M. Recent Advances in Second Near-Infrared Region (NIR-II) Fluorophores and Biomedical Applications. *Front. Chem.* **2021**, *9*, No. 750404.

(3) Shi, T.; Huang, C.; Li, Y.; Huang, F.; Yin, S. NIR-II Phototherapy Agents with Aggregation-Induced Emission Characteristics for Tumor Imaging and Therapy. *Biomater.* **2022**, *285*, No. 121535.

(4) An, D.; Fu, J.; Zhang, B.; Xie, N.; Nie, G.; Ågren, H.; Qiu, M.; Zhang, H. NIR-II Responsive Inorganic 2D Nanomaterials for Cancer Photothermal Therapy: Recent Advances and Future Challenges. *Adv. Funct. Mater.* **2021**, *31*, 2101625.

(5) Liu, B. M.; Guo, X. X.; Huang, L.; Zhou, R. F.; Zou, R.; Ma, C. G.; Wang, J. A Super-Broadband NIR Dual-Emitting Mg_2SnO_4:Cr^{3+},Ni^{2+} Phosphor for Ratiometric Phosphor-Converted NIR Light Source Applications. *Adv. Mater. Technol.* **2023**, *8*, 2201181.

(6) Nair, G. B.; Swart, H.; Dhoble, S. A Review on the Advancements in Phosphor-Converted Light Emitting Diodes (pc-LEDs): Phosphor Synthesis, Device Fabrication and Characterization. *Prog. Mater. Sci.* **2020**, *109*, No. 100622.

(7) Zhao, F.; Song, Z.; Liu, Q. Advances in Chromium-Activated Phosphors for Near-Infrared Light Sources. *Laser Photonics Rev.* **2022**, *16*, 2200380.

(8) Chang, C. Y.; Majewska, N.; Chen, K. C.; Huang, W. T.; Lesniewski, T.; Leniec, G.; Kaczmarek, S. M.; Pang, W. K.; Peterson, V. K.; Cherng, D. H.; Lu, K. M.; Mahlik, S.; Liu, R. S. Broadening Phosphor-Converted Light-Emitting Diode Emission: Controlling Disorder. *Chem. Mater.* **2022**, *34*, 10190−10199.

(9) Cai, H.; Liu, S.; Song, Z.; Liu, Q. Tuning Luminescence from NIR-I to NIR-II in Cr^{3+}-Doped Olivine Phosphors for Nondestructive Analysis. *J. Mater. Chem. C* **2021**, *9*, 5469−5477.

(10) Yuan, L.; Jin, Y.; Wu, H.; Deng, K.; Qu, B.; Chen, L.; Hu, Y.; Liu, R. S. Ni^{2+}-Doped Garnet Solid-Solution Phosphor-Converted Broadband Shortwave Infrared Light-Emitting Diodes toward Spectroscopy Application. *ACS Appl. Mater. Interfaces* **2022**, *14*, 4265−4275.

(11) Yang, Z.; Zhao, Y.; Zhou, Y.; Qiao, J.; Chuang, Y. C.; Molokeev, M. S.; Xia, Z. Giant Red-Shifted Emission in (Sr,Ba)-Y_2O_4:Eu^{2+} Phosphor Toward Broadband Near-Infrared Luminescence. *Adv. Funct. Mater.* **2022**, *32*, 2103927.

(12) Kumar, G. A.; Pokhrel, M.; Martinez, A.; Dennis, R. C.; Villegas, I. L.; Sardar, D. K. Synthesis and Spectroscopy of Color Tunable Y_2O_2S:Yb^{3+},Er^{3+} Phosphors with Intense Emission. *J. Alloys Compd.* **2012**, *513*, 559−565.

(13) Liu, B. M.; Gu, S. M.; Huang, L.; Zhou, R. F.; Zhou, Z.; Ma, C. G.; Zou, R.; Wang, J. Ultra-Broadband and High-Efficiency Phosphors to Brighten NIR-II Light Source Applications. *Cell Rep. Phys. Sci.* **2022**, *3*, No. 101078.

(14) Zhou, S.; Feng, G.; Wu, B.; Jiang, N.; Xu, S.; Qiu, J. Intense Infrared Luminescence in Transparent Glass-Ceramics containing β-Ga_2O_3:Ni^{2+} Nanocrystals. *J. Phys. Chem. C* **2007**, *111*, 7335−7338.

(15) Gao, Y.; Wang, B.; Liu, L.; Shinozaki, K. Near-Infrared Engineering for Broad-Band Wavelength-Tunable in Biological Window of NIR-II and-III: A Solid Solution Phosphor of $Sr_{1-x}Ca_xTiO_3$:Ni^{2+}. *J. Lumin.* **2021**, *238*, No. 118235.

(16) Wang, C.; Zhang, Y.; Han, X.; Hu, D.; He, D.; Wang, X.; Jiao, H. Energy Transfer Enhanced Broadband Near-Infrared Phosphors: Cr^{3+}/Ni^{2+} Activated $ZnGa_2O_4$−Zn_2SnO_4 Solid Solutions for the Second NIR Window Imaging. *J. Mater. Chem. C* **2021**, *9*, 4583−4590.

(17) Miao, S.; Liang, Y.; Zhang, Y.; Chen, D.; Wang, X. J. Blue LED-Pumped Broadband Short-Wave Infrared Emitter Based on $LiMgPO_4$:Cr^{3+},Ni^{2+} Phosphor. *Adv. Mater. Technol.* **2022**, *7*, 2200320.

(18) Liu, B. M.; Guo, X. X.; Cao, L. Y.; Huang, L.; Zou, R.; Zhou, Z.; Wang, J. A High-Efficiency Blue-LED-Excitable NIR-II-Emitting MgO:Cr^{3+},Ni^{2+} Phosphor for Future Broadband Light Source toward Multifunctional NIR Spectroscopy Applications. *J. Chem. Eng.* **2023**, *452*, No. 139313.

(19) Tsai, Y. T.; Huang, Y. K.; Jiang, Z. F.; Yao, Y.; Lo, P. H.; Chao, Y. C.; Lin, B. H.; Lin, C. C. Cation Substitution-Induced Partial Inversion to Pervade Short-Wave Infrared Light for Improving the Accuracy of Artificial Intelligence Image Recognition System. *ACS Materials Lett.* **2023**, *5*, 738−743.

(20) Zhang, Q.; Liu, D.; Wang, Z.; Dang, P.; Lian, H.; Li, G.; Lin, J. $LaMgGa_{11}O_{19}$:Cr^{3+},Ni^{2+} as Blue-Light Excitable Near-Infrared Luminescent Materials with Ultra-Wide Emission and High External Quantum Efficiency. *Adv. Opt. Mater.* **2023**, *11*, 2202478.

(21) Miao, S.; Liang, Y.; Shi, R.; Wang, W.; Li, Y.; Wang, X. J. Broadband Short-Wave Infrared-Emitting $MgGa_2O_4$:Cr^{3+}, Ni^{2+} Phosphor with Near-Unity Internal Quantum Efficiency and High Thermal Stability for Light-Emitting Diode Applications. *ACS Appl. Mater. Interfaces* **2023**, *15*, 32580−32588.

(22) Yao, L.; Jia, Q.; Yu, S.; Liang, C.; Jiang, J.; Shao, Q. Simultaneous Absorption and Near-Infrared Emission Enhancement of Cr^{3+} Ions in $MgGa_2O_4$ Spinel Oxide via Anionic F-Substitution. *Adv. Opt. Mater.* **2023**, *11*, 2202458.

(23) Rajendran, V.; Chang, C. Y.; Huang, M. H.; Chen, K. C.; Huang, W. T.; Kamiński, M.; Lesniewski, T.; Mahlik, S.; Leniec, G.; Lu, K. M.; Wei, D. H.; Chang, H.; Liu, R. S. Chromium Cluster Luminescence: Advancing Near-Infrared Light-Emitting Diode Design for Next-Generation Broadband Compact Light Sources. *Adv. Opt. Mater.* **2023**, 2302645.

(24) Henderson, B.; Imbusch, G. F. *Optical Spectroscopy of Inorganic Solids*, Vol. *44*. Oxford University Press, 2006.

(25) Yuan, L.; Jin, Y.; Zhu, D.; Mou, Z.; Xie, G.; Hu, Y. Ni^{2+}-Doped Yttrium Aluminum Gallium Garnet Phosphors: Bandgap Engineering for Broad-Band Wavelength-Tunable Shortwave-Infrared Long-Persistent Luminescence and Photochromism. *ACS Sustain. Chem. Eng.* **2020**, *8*, 6543−6550.

(26) Toby, B. H. R Factors in Rietveld Analysis: How Good is Good Enough? *Powder Diffr.* **2006**, *21*, 67−70.

(27) Shannon, R. D. Revised Effective Ionic Radii and Systematic Studies of Interatomic Distances in Halides and Chalcogenides. *Acta Cryst. A* **1976**, *32*, 751−767.
(28) Schwarz, L.; Galazka, Z.; Gesing, T. M.; Klimm, D. On the Influence of Inversion on Thermal Properties of Magnesium Gallium Spinel: Dedicated to the 80th Birthday of Prof. Joachim Bohm. *Cryst. Res. Technol.* **2015**, *50*, 961−966.
(29) Koningsberger, D. C.; Prins, R. *X-Ray Absorption: Principles, Applications, Techniques of EXAFS, SEXAFS and XANES*: United States, 1987.
(30) Yamamoto, T. Assignment of Pre-Edge Peaks in K-edge X-Ray Absorption Spectra of 3*d* Transition Metal Compounds: Electric Dipole or Quadrupole? *X-Ray Spectrometry: An International Journal* **2008**, *37*, 572−584.
(31) Leniec, G. Electron Paramagnetic Resonance: A Technique to Locate the Nearest Environment of Chromium Luminescent Centers. *ACS Appl. Opt. Mater.* **2023**, *1*, 1114−1121.
(32) Rajendran, V.; Fang, M. H.; Huang, W. T.; Majewska, N.; Lesniewski, T.; Mahlik, S.; Leniec, G.; Kaczmarek, S. M.; Pang, W. K.; Peterson, V. K.; Lu, K. M.; Chang, H.; Liu, R. S. Chromium Ion Pair Luminescence: A Strategy in Broadband Near-Infrared Light-Emitting Diode Design. *J. Am. Chem. Soc.* **2021**, *143*, 19058−19066.
(33) Bobrowska, M.; Typek, J.; Leniec, G.; Zolnierkiewicz, G.; Filipek, E.; Prokop, A.; Blonska-Tabero, A. A Novel Look at Magnetism in Ni_2FeVO_6. *IEEE Trans. Magn.* **2022**, *58*, 1−10.
(34) Worsztynowicz, A.; Kaczmarek, S. M.; Bosacka, M.; Mody, V.; Czernuszewicz, R. S. Structural and Magnetic Characterization of the Cr^{3+} and Ni^{2+} Ion Species in $Ni_2CrV_3O_{11}$. *Rev. Adv. Mater. Sci.* **2007**, *14*, 24−32.
(35) Tomono, Y.; Kato, T.; Tanokura, Y. EPR Spectra from Ni^{2+} Pairs in $KZnF_3$ Crystals. *J. Phys. Soc. Jpn.* **1984**, *53*, 773−779.
(36) Bleaney, B. Anomalous Paramagnetism of Copper Acetate. *Rev. Mod. Phys.* **1953**, *25*, 161.
(37) Ellis, R. S. *Entropy, Large Deviations, and Statistical Mechanics*, Vol. *1431*. Taylor & Francis, 2006.
(38) Sayler, R. I.; Hunter, B. M.; Fu, W.; Gray, H. B.; Britt, R. D. EPR Spectroscopy of Iron-and Nickel-Doped [ZnAl]-Layered Double Hydroxides: Modeling Active Sites in Heterogeneous Water Oxidation Catalysts. *J. Am. Chem. Soc.* **2020**, *142*, 1838−1845.
(39) Rajendran, V.; Chen, K. C.; Huang, W. T.; Kamiński, M.; Grzegorczyk, M.; Mahlik, S.; Leniec, G.; Lu, K. M.; Wei, D. H.; Chang, H.; Liu, R. S. Unraveling Luminescent Energy Transfer Pathways: Futuristic Approach of Miniature Shortwave Infrared Light-Emitting Diode Design. *ACS Energy Lett.* **2023**, *8*, 2395−2400.
(40) Suzuki, T.; Murugan, G. S.; Ohishi, Y. Spectroscopic Properties of a Novel Near-Infrared Tunable Laser Material $Ni:MgGa_2O_4$. *J. Lumin.* **2005**, *113*, 265−270.
(41) Pappalardo, R.; Wood, D. L.; Linares, R. C., Jr Optical Absorption Spectra of Ni-Doped Oxide Systems. *J. Chem. Phys.* **1961**, *35*, 1460−1478.
(42) Koetke, J.; Huber, G.; Petermann, K. Spectroscopy of Ni^{2+}-Doped Garnets and Perovskites for Solid State Lasers. *J. Lumin.* **1991**, *48*, 564−568.

https://doi.org/10.1021/acs.chemmater.4c00438
Chem. Mater. 2024, 36, 3941−3948